



# Visible-light-induced oxidative alkene difunctionalization to access $\alpha$ -sulfonyloxy ketones catalyzed by oxygen-vacancy-rich $\text{Nb}_2\text{O}_5$

Tao Song<sup>a,b,c,1</sup>, Chun Wang<sup>d,1</sup>, Yinpan Zhang<sup>a,b,c</sup>, Xiaoling Shi<sup>a,b,c</sup>, Yafei Li<sup>d,\*</sup>,  
Yong Yang<sup>a,b,c,\*\*</sup>

<sup>a</sup> CAS Key Laboratory of Bio-based Materials, Qingdao Institute of Bioenergy and Bioprocess Technology, Chinese Academy of Sciences, Qingdao 266101, China

<sup>b</sup> Shandong Energy Institute, Qingdao 266101, China

<sup>c</sup> Qingdao New Energy Shandong Laboratory, Qingdao 266101, China

<sup>d</sup> School of Chemistry and Materials Science, Nanjing Normal University, Nanjing 210023, China

## ARTICLE INFO

### Keywords:

Alkene difunctionalization

$\text{Nb}_2\text{O}_5$

Photocatalysis

Oxygen vacancy engineering

$\alpha$ -sulfonyloxy ketones

## ABSTRACT

Herein, we report an oxygen vacancy (OVs)-rich  $\text{Nb}_2\text{O}_5$  semiconductor (OVs-N- $\text{Nb}_2\text{O}_5$ ) as a bifunctional heterogeneous photocatalyst for unprecedented synthesis of  $\alpha$ -sulfonyloxy ketones via oxidative alkene difunctionalization with sodium sulfinate under visible light irradiation and ambient conditions. A broad set of aromatic and aliphatic alkenes was efficiently difunctionalized into diverse  $\alpha$ -sulfonyloxy ketones in high yields with a good functional group tolerance. The catalyst OVs-N- $\text{Nb}_2\text{O}_5$  is highly stable and could be easily recovered for at least 6 successive recycles with maintaining photoactivity and selectivity. Experimental and theoretical investigations reveal that the presence of OVs not only accelerates the separation and transfer of photogenerated electron-hole pairs, but also promotes  $\text{O}_2$  adsorption and activation to form long-lived superoxide anion radical ( $\text{O}_2^{\bullet-}$ ), which greatly boosts the reaction and modulates the reaction pathways together with the intrinsic Lewis acid sites, thereby resulting in an improved reaction activity and excellent selectivity to the desired product.

## 1. Introduction

As an emerging alternative to traditionally energy-intensive thermochemical organic transformations, photocatalysis powered by visible light irradiation has attracted increasing attention to synthesize highly value-added and even complex organic compounds over the past decade [1]. Transition metal complexes (e.g.,  $\text{Ru}(\text{bpy})_3^{2+}$  [2], *fac*- $\text{Ir}(\text{ppy})_3$  [3],  $\text{Cu}(\text{dpa})_2^+$  [4], gold complexes [5]) and organic dyes (e.g., Methylene Blue [6], Eosin Y [7], 4CzIPN [8], pyrylium or acridinium salts [9]) have been extensively investigated as photocatalysts for a broad set of photoredox transformations. However, despite great achievements, these homogeneous molecular photocatalysts suffer from the key issues including (1) poor compatibility. They are very sensitive to strong acidic or basic conditions, or are prone to react with strong nucleophiles, electrophiles, or even reactive radical intermediates, generally leading to the change of their photoelectronic properties or direct decomposition, thereby losing their photoactivity. (2) non-reusability. The

difficulty in their separation from the reaction product along with tedious and high-energy input process causes a heavy burden in both economy and environment, significantly hampering their practical potential.

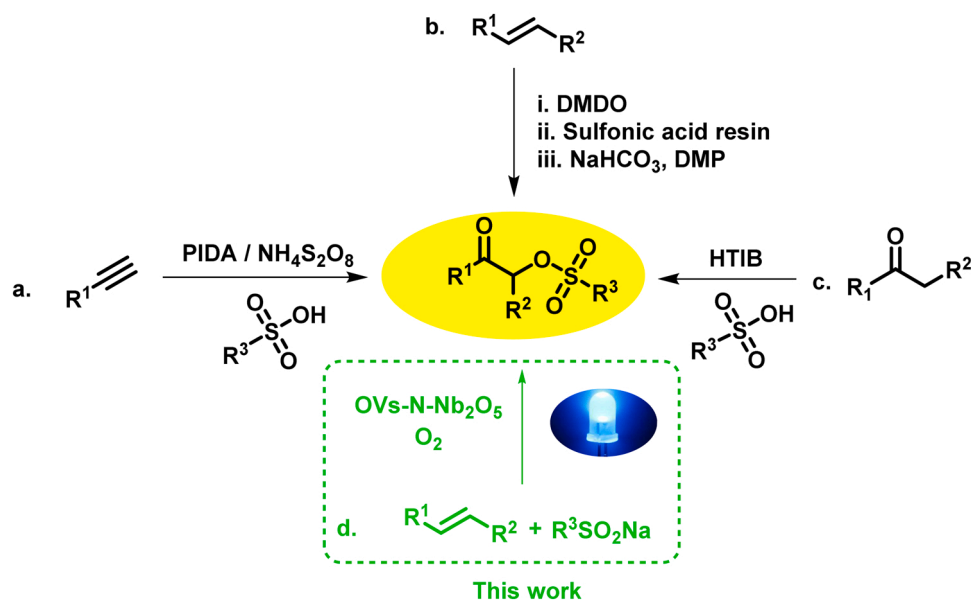
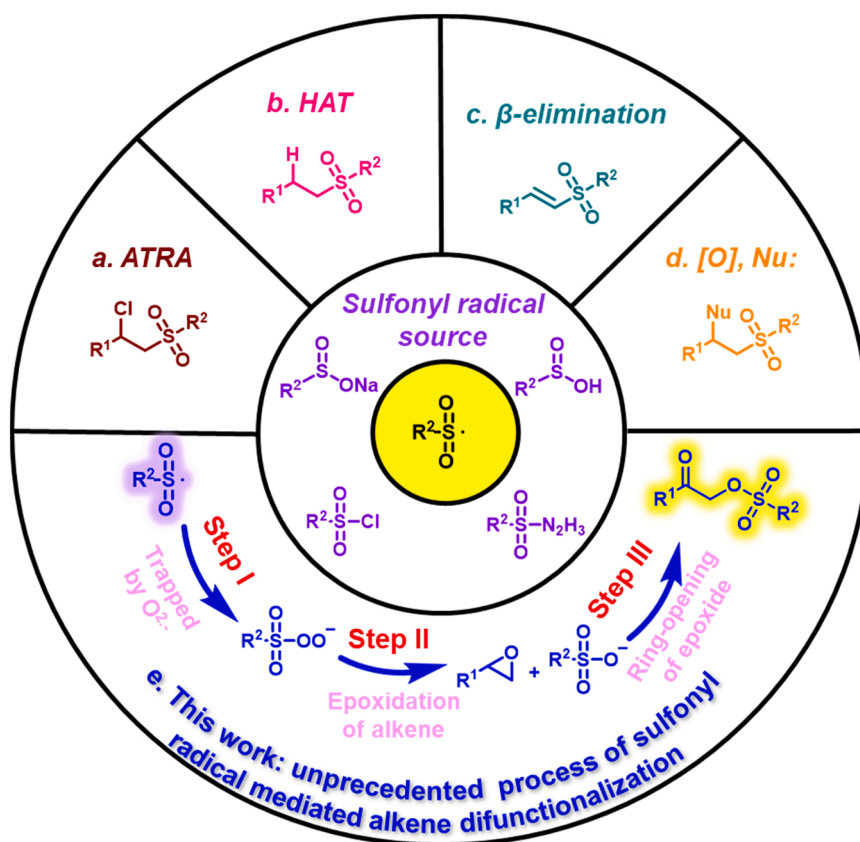
In sharp contrast, semiconductor materials (e.g.,  $\text{TiO}_2$ ,  $\text{Nb}_2\text{O}_5$ , mesoporous graphitic carbon nitride (mpg- $\text{C}_3\text{N}_4$ )) as heterogeneous photocatalysts are photochemically stable to tolerate harsh conditions and can be readily recovered for reuse [10]. Different from molecular photocatalysts, the photoredox reaction simultaneously occurs on the surface of semiconductor via photogenerated electron-hole pairs upon light illumination. As such, the morphology and local surface structure of semiconductors profoundly affect the photoreaction efficiency and selectivity via adjusting electron-hole transfer dynamics or stabilizing catalytic sites [11]. More importantly, the bandgap between valence band (VB) and conduction band (CB) of semiconductors is easily adjustable to form an appropriate redox window to meet a broad spectrum of organic reactions via heteroatom doping or formation of

\* Corresponding author.

\*\* Corresponding author at: CAS Key Laboratory of Bio-based Materials, Qingdao Institute of Bioenergy and Bioprocess Technology, Chinese Academy of Sciences, Qingdao 266101, China.

E-mail addresses: [liyafei@nynu.edu.cn](mailto:liyafei@nynu.edu.cn) (Y. Li), [yangyong@qibebt.ac.cn](mailto:yangyong@qibebt.ac.cn) (Y. Yang).

<sup>1</sup> These authors contributed equally.

Scheme 1. Strategies for synthesis of  $\alpha$ -sulfonyloxy ketones.

Scheme 2. Reaction pathways of sulfonyl radical with alkenes.

heterojunction structure [12]. In addition, the inherently acidic or basic property of some specific semiconductors makes them more attractive in organic transformations, which might change the adsorption and activation modes of substrate or reaction intermediate on their surface, especially for those reactions with necessary of acid or base assisting, such as hydrolysis reaction, dehydration reaction, or epoxide ring-opening reaction [13]. However, a synergy of photo- and acid-catalysis in one catalyst entity for organic transformations has been

paid less attention.

$\alpha$ -sulfonyloxy ketones are important strategic precursors in organic synthesis owing to the strong electron-withdrawing and high leaving properties of sulfonyloxy group [14]. A variety of biologically important heterocyclic compounds has been successfully synthesized starting from  $\alpha$ -sulfonyloxy ketones via either direct nucleophiles attachment, formation of  $\alpha$ -keto carbocations, oxy-allyl cations; or from *o*-alkynylbenzenesulfonamides via difunctionalizations of alkynes [15].

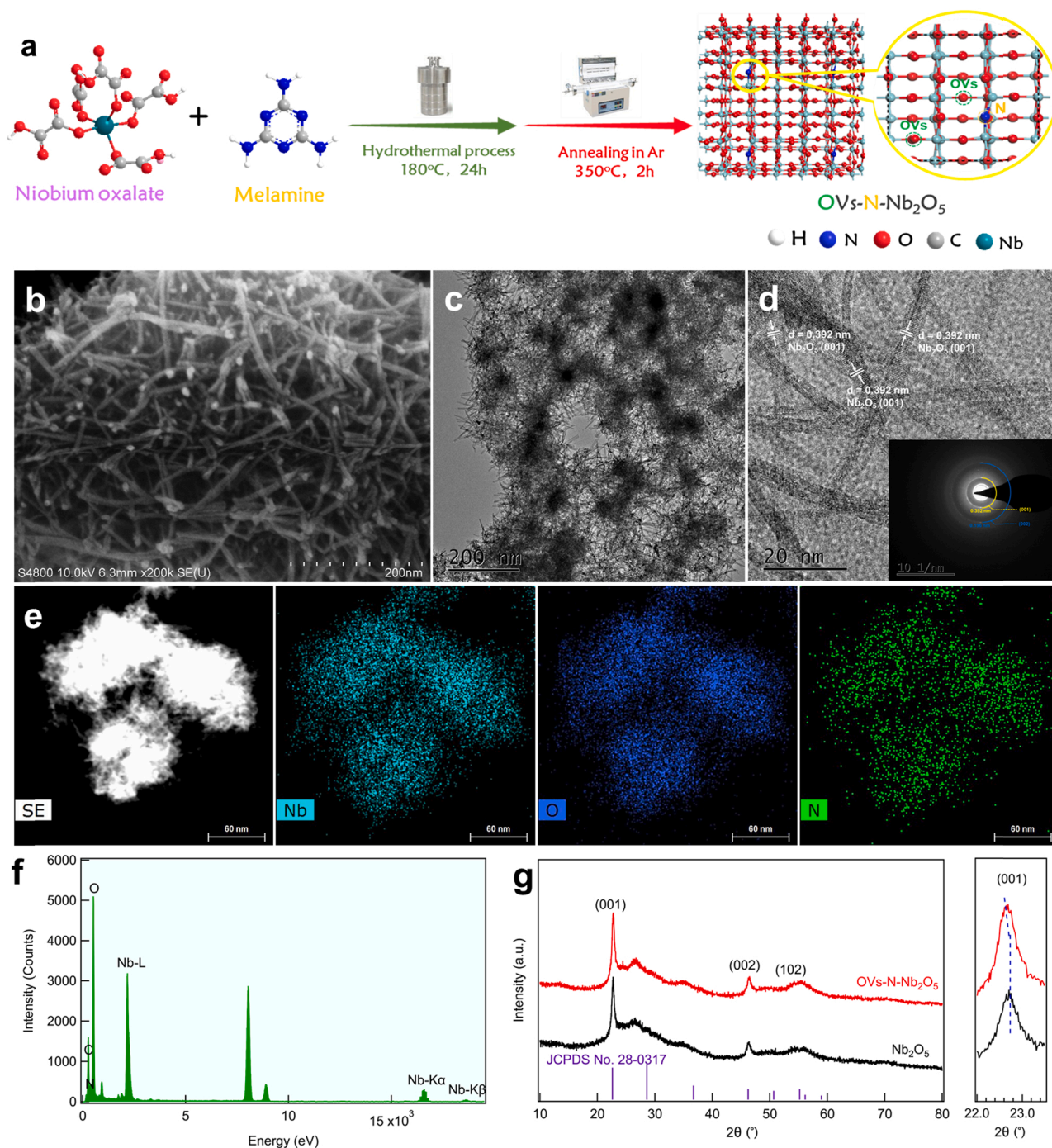


**Fig. 1.** (a) Illustrative procedure for preparation of OV5-N-Nb<sub>2</sub>O<sub>5</sub>. (b) SEM, (c) TEM, and (d) HR-TEM images with an inset SEAD pattern of OV5-N-Nb<sub>2</sub>O<sub>5</sub>. (e) HAADF STEM image and corresponding EDX mappings of Nb, O, and N elements. (f) EDS spectrum of OV5-N-Nb<sub>2</sub>O<sub>5</sub>. (g) XRD patterns of OV5-N-Nb<sub>2</sub>O<sub>5</sub> and the pristine Nb<sub>2</sub>O<sub>5</sub>.

Currently, synthesis of  $\alpha$ -sulfonyloxy ketones predominantly relies on organic hypervalent iodine reagents (e.g., iodobenzene diacetate (PIDA), HTIB (Koser's reagent)) or their precursors (peroxides and iodides) mediated oxysulfonyloxylation of alkenes, alkynes, or ketones derivatives with sulfonic acids together with stoichiometric amounts of toxic oxidants such as dimethyldioxolone (DMDO), (NH<sub>4</sub>)<sub>2</sub>S<sub>2</sub>O<sub>8</sub> [15a-17] (Scheme 1). However, the issue of limited substrate scope with environmentally unfriendly conditions hampers their application. Radical-mediated alkene difunctionalization with varying sulfonyl radical precursors (e.g., sodium sulfinate, sulfonylhydrazide, sulfinic acid, sulfonyl chloride) catalyzed by transition metals, metal-free, or

homogeneous photocatalysts have been intensively explored [18-21]. Unfortunately, in these cases,  $\alpha$ -sulfone substituted products other than  $\alpha$ -sulfonyloxy ketones are generally delivered, in which the addition of in-situ generated sulfonyl radical to alkene forms a carbon centered radical followed by either atom transfer radical addition (ATRA) (Scheme 2a) [18], hydrogen atom transfer (HAT) (Scheme 2b) [19],  $\beta$ -elimination (Scheme 2c) [20], or attack by nucleophiles upon its oxidation to carbon cation (Scheme 2d) [21]. We then question whether it would be possible for the synthesis of  $\alpha$ -sulfonyloxy ketones from readily available alkenes instead of alkynes or ketone derivatives via visible-light induced radical-mediated difunctionalization, which has

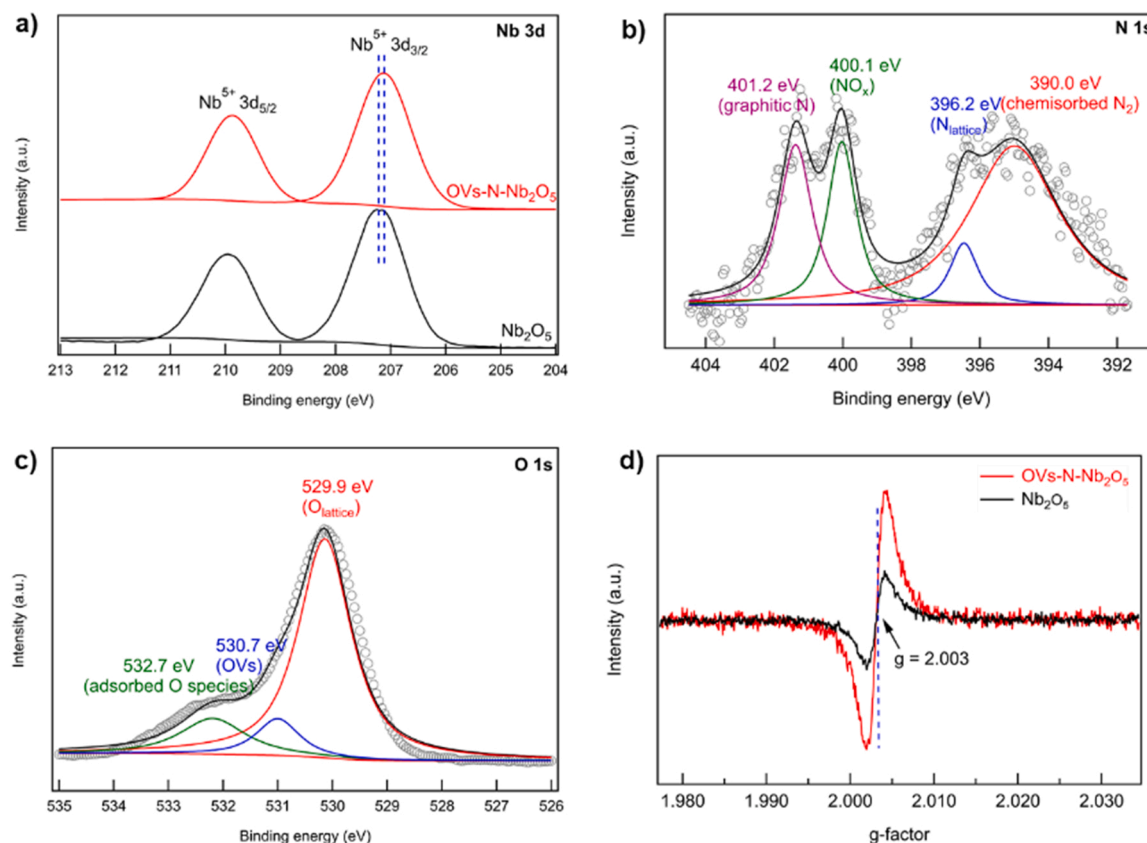


Fig. 2. (a) High-resolution XPS spectra of Nb 3d for OV-N-Nb<sub>2</sub>O<sub>5</sub> and the pristine Nb<sub>2</sub>O<sub>5</sub>. (b) N 1s and (c) O 1s XPS spectra for OV-N-Nb<sub>2</sub>O<sub>5</sub>. (d) EPR spectra of OV-N-Nb<sub>2</sub>O<sub>5</sub> and the pristine Nb<sub>2</sub>O<sub>5</sub>.

rarely been reported thus far.

In this work, we report an unprecedented synthetic route for sustainable and expedient synthesis of  $\alpha$ -sulfonyloxy ketones via radical-mediated oxidative alkene difunctionalization with sodium sulfinate (Scheme 1d). The reaction was catalyzed by a Lewis acidic and oxygen vacancy-rich Nb<sub>2</sub>O<sub>5</sub> semiconductor (labeled as OV-N-Nb<sub>2</sub>O<sub>5</sub>) under visible light irradiation and ambient conditions in a synergistic and cascade manner (Scheme 2e). A diverse set of readily available alkenes could be efficiently difunctionalized in good to high yields with good functional group compatibility. Moreover, the catalyst OV-N-Nb<sub>2</sub>O<sub>5</sub> could be readily recovered and reused for at least 6 times with conserved activity and selectivity. Experimental and theoretical investigations reveal that the synergy of OVs and Lewis acid sites on the surface of Nb<sub>2</sub>O<sub>5</sub> modulates reaction pathway and improves reaction efficiency. The OVs substantially benefit for O<sub>2</sub> adsorption and activation to selectively generate a long-lived O<sub>2</sub><sup>•−</sup> and then favor the formation of strong epoxidizing sulfonyl peroxide anion, while the intrinsic Lewis acid sites facilitate the key intermediate epoxide ring-opening to afford the target products.

## 2. Experimental section

### 2.1. Materials

Niobium oxalate, melamine, ethanol, alkenes or its raw materials were purchased commercially from Sigma-Aldrich, or Aladdin and used as received without further purification.

### 2.2. Preparation of OV-N-Nb<sub>2</sub>O<sub>5</sub>

Niobium oxalate (1.076 g, 2 mmol) was dissolved in 30 mL deionized water/ethanol mixture solvent (volume ratio of 3:1) at 60 °C,

followed by addition of 5 mL aqueous solution of melamine (45.6 mg, 0.33 mmol). The mixture solution was transferred to a 100 mL Teflon-inner stainless-steel autoclave, and sealed and heated at 180 °C for 24 h. When the hydrothermal process was completed, the resulting solids were washed by centrifugation, and dried under vacuum at 60 °C for 12 h. After that, the solids were grinded to fine powder and placed in a tubular furnace for calcination at 350 °C for 3 h with a heating rate of 5 °C min<sup>−1</sup> from room temperature under N<sub>2</sub> atmosphere. The as-obtained solid was denoted as OV-N-Nb<sub>2</sub>O<sub>5</sub>. A similar procedure was used for the preparation of the pristine Nb<sub>2</sub>O<sub>5</sub> without addition of melamine.

### 2.3. Photocatalytic alkene difunctionalization to synthesize $\alpha$ -sulfonyloxy ketones

A 25 mL sealing tube was charged with a magnetic stirring bar, alkene (0.2 mmol), OV-N-Nb<sub>2</sub>O<sub>5</sub> (20 mg), sodium sulfinate (0.6 mmol, 3 equiv.), benzonitrile (2 mL). The reaction was stirred for 24 h at room temperature under 1 atm O<sub>2</sub> atmosphere with blue LED light (5 W, 450 nm) irradiation. After completion of the reaction, the reaction mixture was filtered and analyzed by NMR to determine conversion and selectivity using 4-nitroacetophenone as an internal standard. The products were purified by column chromatography and structurally confirmed by NMR.

### 2.4. DFT calculation

All the theoretical calculations were performed via the Vienna ab initio simulation package (VASP) in the framework of density functional theory (DFT). The projector augmented wave (PAW) approach was chosen to describe the electron ion interaction. The generalized gradient approximation (GGA) expressed by the PBE functional was adopted to describe the exchange-correlation term. In computation, van der Waals



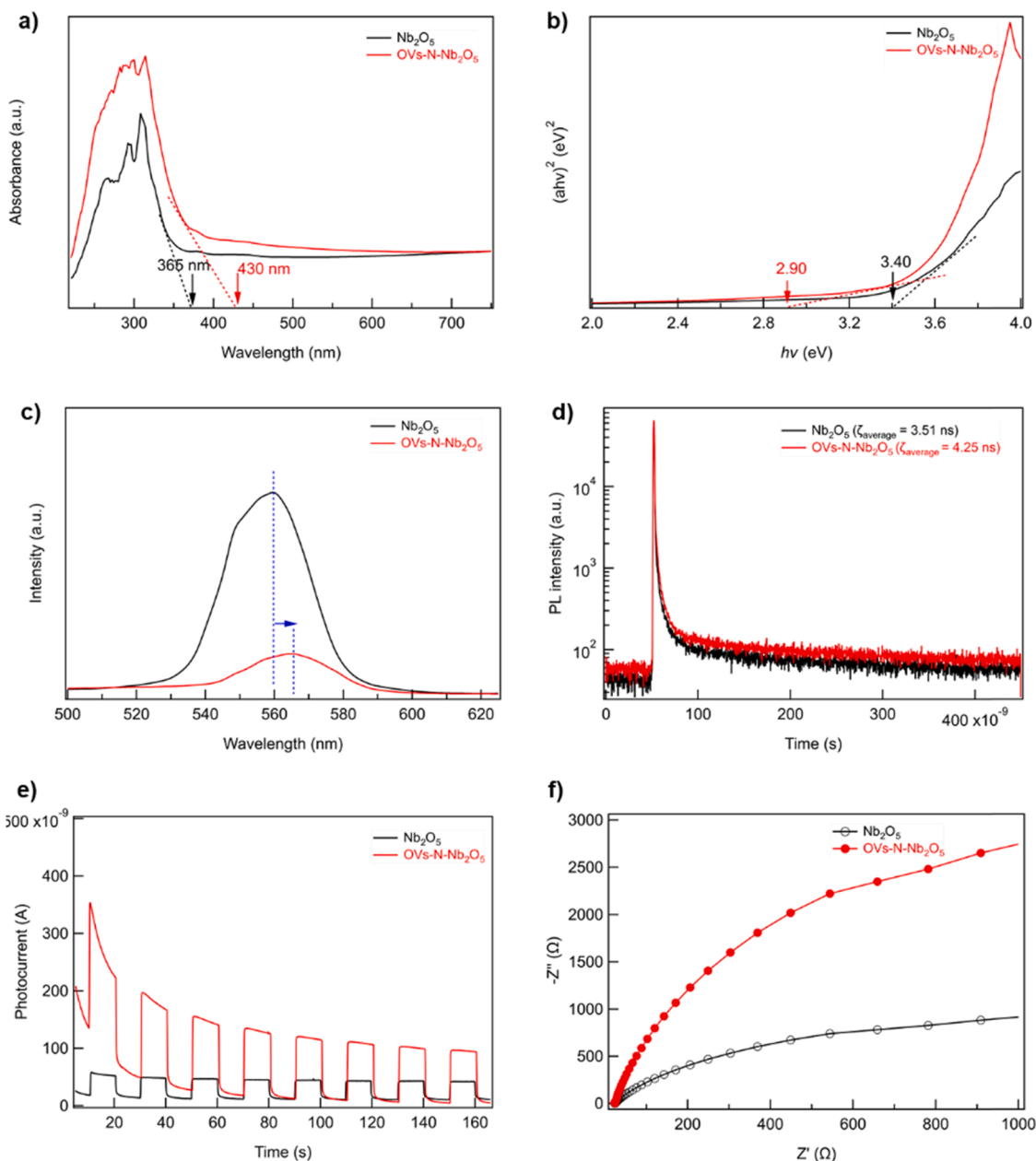


**Fig. 3.** (a) Diffuse reflectance UV/Vis spectra (DRS), (b) Tauc plots for bandgap energy estimation, (c) steady-state PL spectra, (d) time-resolved PL decay spectra, (e) transient photocurrent response, and (f) EIS Nyquist plots of OV-N-Nb<sub>2</sub>O<sub>5</sub> and the pristine Nb<sub>2</sub>O<sub>5</sub>.

interactions were included by using DFT-D3 Method. The convergence criteria of energy and force were less than  $10^{-4}$  eV and 0.05 eV/Å, respectively. The Brillouin zone was sampled with an  $1 \times 3 \times 3$  Monkhorst-Park k-points grid and a 450 eV cutoff for the plane-wave basis set was adopted in all computations. The three-layer  $p(3 \times 3)$  surface slab for the Nb<sub>2</sub>O<sub>5</sub> (001) surfaces and N atoms modified Nb<sub>2</sub>O<sub>5</sub> surfaces with oxygen vacancies (OV-N-Nb<sub>2</sub>O<sub>5</sub>) were constructed. The vacuum space along the x-direction was set at least 20 Å to eliminate the interaction between neighboring slabs. The adsorption energy of species X on the surface,  $E_{\text{ads}}(X)$ , was calculated with.

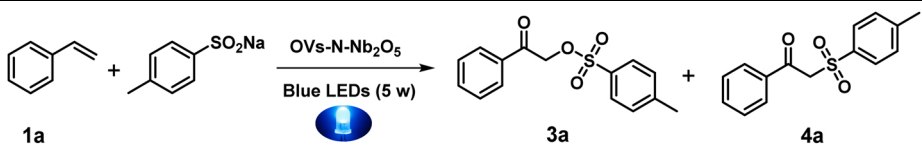
$$E_{\text{ads}}(X) = E_{X/\text{slab}} - E_{\text{slab}} - E_X$$

Here,  $E_{X/\text{slab}}$  refers to the total energy of adsorption system,  $E_{\text{slab}}$  shows the energy of the clean surface, and  $E_X$  is the energy of the gas molecule X. A negative  $E_{\text{ads}}(X)$  value indicates an exothermic adsorption process.

## 2.5. Characterization

The X-ray diffraction (XRD) patterns were obtained on a Bruker D8 Advance diffractometer equipped with Cu Kα radiation ( $\lambda = 1.5147$  Å). Transmission electron microscope (TEM) images were recorded using a H-7600, high-resolution TEM (HRTEM) and scanning transmission electron microscope (STEM) images were recorded using Tecnai G2 F30. Nitrogen adsorption-desorption data were obtained on a Micromeritics ASAP 2020 static volumetric sorption analyzer. The specific surface area of the samples was calculated by the Brunauer-Emmet-Teller (BET) method. The micropore volume was calculated by t-plot method. The pore size distributions were determined by non-local density functional theory (NLDFT). Inductively coupled plasma atomic emission spectroscopy (ICP-AES) was conducted on a PerkinElmer Optima 5300 DV instrument. The X-ray photoelectron spectroscopy (XPS) analyses were conducted on an ESCALAB 250Xi (Thermo Scientific, UK) instrument using an Al Kα line source. All the binding energies obtained were

**Table 1**  
Optimization of the reaction conditions<sup>a</sup>.



Entry	Solvent	Time	Conv./% <sup>b</sup>	Selec./% <sup>b</sup>	3a	4a
1	BTF	12 h	57	87	13	
2	CH <sub>3</sub> CN	12 h	40	78	22	
3	MeOH	12 h	13	6	94	
4	DMF	12 h	15	27	73	
5	CH <sub>3</sub> CN/H <sub>2</sub> O (1/1)	12 h	43	32	68	
6	BTF/H <sub>2</sub> O (1/1)	12 h	41	45	55	
7	1,4-Dioxane/H <sub>2</sub> O (1/1)	12 h	41	0	100	
8	BTF	24 h	100	86	14	
9 <sup>c</sup>	BTF	24 h	0	0	0	
10 <sup>d</sup>	BTF	24 h	0	0	0	
11 <sup>e</sup>	BTF	24 h	0	0	0	
12 <sup>f</sup>	BTF	24 h	45	81	19	
13 <sup>g</sup>	BTF	60 h	100	80	20	

<sup>a</sup> Reaction conditions: styrene (0.2 mmol), sodium *p*-toluenesulfonate (0.6 mmol), OV<sub>s</sub>-N-Nb<sub>2</sub>O<sub>5</sub> (20 mg), solvent (2 mL), atmospheric O<sub>2</sub>, room temperature.

<sup>b</sup> Determined by NMR.

<sup>c</sup> Ar atmosphere.

<sup>d</sup> without LEDs.

<sup>e</sup> without OV<sub>s</sub>-N-Nb<sub>2</sub>O<sub>5</sub>.

<sup>f</sup> Nb<sub>2</sub>O<sub>5</sub> was used instead. <sup>g</sup>styrene (5 mmol), sodium *p*-toluenesulfonate (15 mmol), OV<sub>s</sub>-N-Nb<sub>2</sub>O<sub>5</sub> (500 mg), BTF (50 mL).

calibrated based on the C 1 s peak at 284.8 eV. The UV-Vis diffuse reflection spectroscopy (UV-DRS) profiles were recorded at room temperature with a wavelength range of 300–800 nm using a PerkinElmer Lambda 365 UV-Vis spectrophotometer with BaSO<sub>4</sub> (spectroscopy grade) as the reference. According to the Kubelka-Munk theory, Tauc plots of a direct semiconductor can be drawn by plotting  $[F(R) \cdot h\nu]^2$  vs  $h\nu$  (incident photo energy), where  $F(R) = (1-R)^2/(2R)$  and  $R$  is the measured reflectance. Photoluminescence (PL) spectra was obtained on a Hitachi F-4600 spectrofluorometer with the excitation wavelength at 380 nm. Time resolved photoluminescence (TRPL) spectra decay was conducted using FluoroMax-4 P (Horiba Jobin Yvon). Fourier Transform Infrared Spectroscopy (FT-IR) was conducted on the Nicolet iN10 IR Microscope (Thermo Fisher, USA). Electron paramagnetic resonance (EPR) signals were recorded on a JES-FA200 spectrometer at 25 °C. For superoxide anion radical (O<sub>2</sub><sup>•-</sup>), 2 mg sample and DMPO (100 mM) was dispersed in 5 mL CH<sub>3</sub>OH, the free radical tested reaction was conducted under flat pool; for oxygen vacancies (OVs), 2 mg sample was dispersed in 5 mL CH<sub>3</sub>OH under anaerobic atmosphere, the free radical reaction was conducted under flat pool. Photoelectrochemical performances measurements were recorded employing an electrochemical analyzer (CHI660E, Shanghai Chenhua electrochemical workstation). Gas chromatography analysis was performed on an Shimadzu Nexis GC-2030 instrument with a flame ionization detector (FID) and an HP-5MS capillary column (30 m, 0.25 mm i.d., 0.25 μm film thicknesses) using helium as the carrier gas. Gas chromatography-mass spectrometry analysis was carried out on an Agilent HP-7890 instrument with an Agilent HP-5975 with triple-axis detector and HP-5 capillary column using helium carrier gas. NMR spectra were from a Bruker DRX-400, or DRX-600, instrument and calibrated using residual non-deuterated solvent (CDCl<sub>3</sub>: δ<sub>H</sub> = 7.26 ppm, δ<sub>C</sub> = 77.16 ppm; C<sub>6</sub>D<sub>6</sub>: δ<sub>H</sub> = 7.16 ppm, δ<sub>C</sub> = 128.06 ppm) as an internal reference.

### 3. Results and discussion

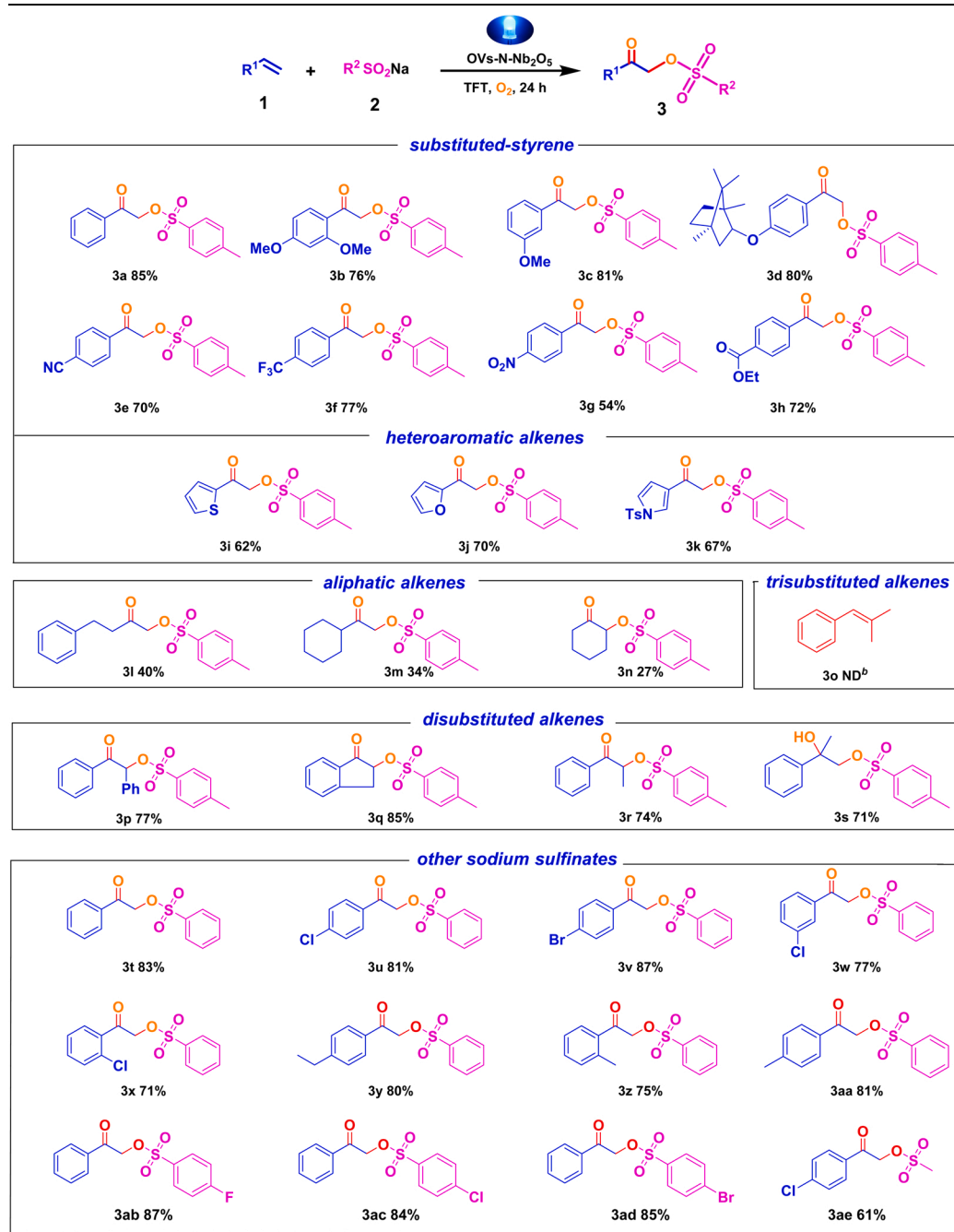
#### 3.1. Characterization of OV<sub>s</sub>-N-Nb<sub>2</sub>O<sub>5</sub>

As well-documented, heteroatom doping has proven to be an effective strategy to tune the photoelectrochemical properties of the existing

semiconductor materials and even to induce defects or vacancies on their surface or in their lattice [11,12]. In this work, we adopted melamine as N source to dope Nb<sub>2</sub>O<sub>5</sub> semiconductor. The catalyst OV<sub>s</sub>-N-Nb<sub>2</sub>O<sub>5</sub> was prepared by hydrothermal process of a mixture of niobium oxalate and melamine followed by calcination at 350 °C for 3 h under nitrogen atmosphere as shown in Fig. 1a. For comparison, the pristine Nb<sub>2</sub>O<sub>5</sub> without N-doping was synthesized via the same procedure to OV<sub>s</sub>-N-Nb<sub>2</sub>O<sub>5</sub> with exception of melamine addition. Scanning electron microscopy (SEM) images (Fig. 1b) reveal that the as-prepared OV<sub>s</sub>-N-Nb<sub>2</sub>O<sub>5</sub> has a nanorod morphology with rough surface in length of 40–70 nm and diameter of 4–6 nm. Transmission electron microscopy (TEM) images (Fig. 1c) verify a random overlapping of nanorods, and high-resolution TEM (HR-TEM) image (Fig. 1d) demonstrates the nanorods with well-resolved lattice fringe spacing of 0.392 nm that corresponds to the (001) crystal planes of the hexagonal phase Nb<sub>2</sub>O<sub>5</sub>. This was further confirmed by the selected-area electron diffraction (SEAD) pattern (Fig. 1d, inset) with typical concentric circles for the Nb<sub>2</sub>O<sub>5</sub> phase. The corresponding energy dispersive X-ray (EDX) elemental mappings (Fig. 1e) disclose the uniform distribution of the Nb, O, and N elements, which is further confirmed by EDS analysis (Fig. 1f). The X-ray diffraction (XRD) pattern (Fig. 1g) for the as-prepared OV<sub>s</sub>-N-Nb<sub>2</sub>O<sub>5</sub> shows the diffraction peaks at 22.6°, 46.2°, 55.2°, indexing to the (001), (002), and (102) lattice planes of the hexagonal Nb<sub>2</sub>O<sub>5</sub> phase (JCPDS# 28-0317), which is good agreement with HR-TEM observation. Of note, a slight negative shift in the (001) plane diffraction peak in OV<sub>s</sub>-N-Nb<sub>2</sub>O<sub>5</sub> was observed compared with the pristine Nb<sub>2</sub>O<sub>5</sub>, suggesting the N atoms substitution in the lattice. No impurities corresponding to other niobium oxide phases were detected. N<sub>2</sub> sorption measurement (Fig. S1, Table S1) shows OV<sub>s</sub>-N-Nb<sub>2</sub>O<sub>5</sub> has a large specific surface area of 245.5 m<sup>2</sup> g<sup>-1</sup> with a hierarchically micro-, meso-, and macro-pores, which are beneficial to mass diffusion and carriers transport. No discrepancy in the morphology, specific surface area, and hierarchical porous structure was observed between OV<sub>s</sub>-N-Nb<sub>2</sub>O<sub>5</sub> and the pristine Nb<sub>2</sub>O<sub>5</sub> (Fig. S2, Table S1), indicating that N-doping has a negligible impact on the intrinsically porous structure. Besides, 1.12 wt% of N was doped into the Nb<sub>2</sub>O<sub>5</sub> lattice by elemental analysis.

The chemical state and surface composition of OV<sub>s</sub>-N-Nb<sub>2</sub>O<sub>5</sub> was

**Table 2**  
Substrate scope for synthesis of  $\alpha$ -sulfonyloxy ketones.<sup>a</sup>



<sup>a</sup>Reaction conditions: alkene (0.2 mmol), sodium sulfinate (0.6 mmol), OV-N-Nb<sub>2</sub>O<sub>5</sub> (20 mg), TBT (2 mL), atmospheric O<sub>2</sub>, blue LEDs (5 W, 450 nm), room temperature, 24 h. <sup>b</sup>No detected. Isolated yields are given.

evaluated by X-ray photoelectron spectroscopy (XPS). The Nb 3d spectrum (Fig. 2a) shows two intense peaks located at 209.7 and 207.1 eV, corresponding to 3d<sub>5/2</sub> and 3d<sub>3/2</sub> states of Nb (V), respectively. A slight negative shift in Nb 3d binding energy was observed compared with the pristine Nb<sub>2</sub>O<sub>5</sub>, which is most likely attributable to the less electronegative N substitution in the lattice and formation of N-Nb bond [22]. The N 1s XPS spectrum (Fig. 2b) is deconvoluted into four peaks. Of them, the peaks centered at 395.0 and 396.2 eV are assignable to the chemisorbed N<sub>2</sub><sup>[10 h]</sup> and substitutional N in the lattice of Nb<sub>2</sub>O<sub>5</sub> [22], respectively. Besides, another two peaks located at 400.4 and 401.2 eV were also observed, which are corresponding to the oxidized N in the form of NO<sub>x</sub> species on the surface of Nb<sub>2</sub>O<sub>5</sub> and partial formation of

graphitic N<sup>[10 h]</sup>, respectively. The O 1s spectrum (Fig. 2c) could be deconvoluted into three peaks centered at 529.9, 530.7, and 532.4 eV, which are assignable to lattice oxygen atoms, oxygen vacancies (OVs), and surface adsorbed oxygen species, respectively [23a]. The electron paramagnetic resonance (EPR) experiment (Fig. 2d) shows a characteristic signal at g = 2.003, which is attributed to OVs, further confirming the formation of OVs [22]. Notably, the OVs signal intensity is markedly increased upon doping with N atoms in comparison with the pristine Nb<sub>2</sub>O<sub>5</sub>. All results clearly indicate that N atoms were successfully doped into the lattice of Nb<sub>2</sub>O<sub>5</sub> and simultaneously induced the abundant formation of OVs.

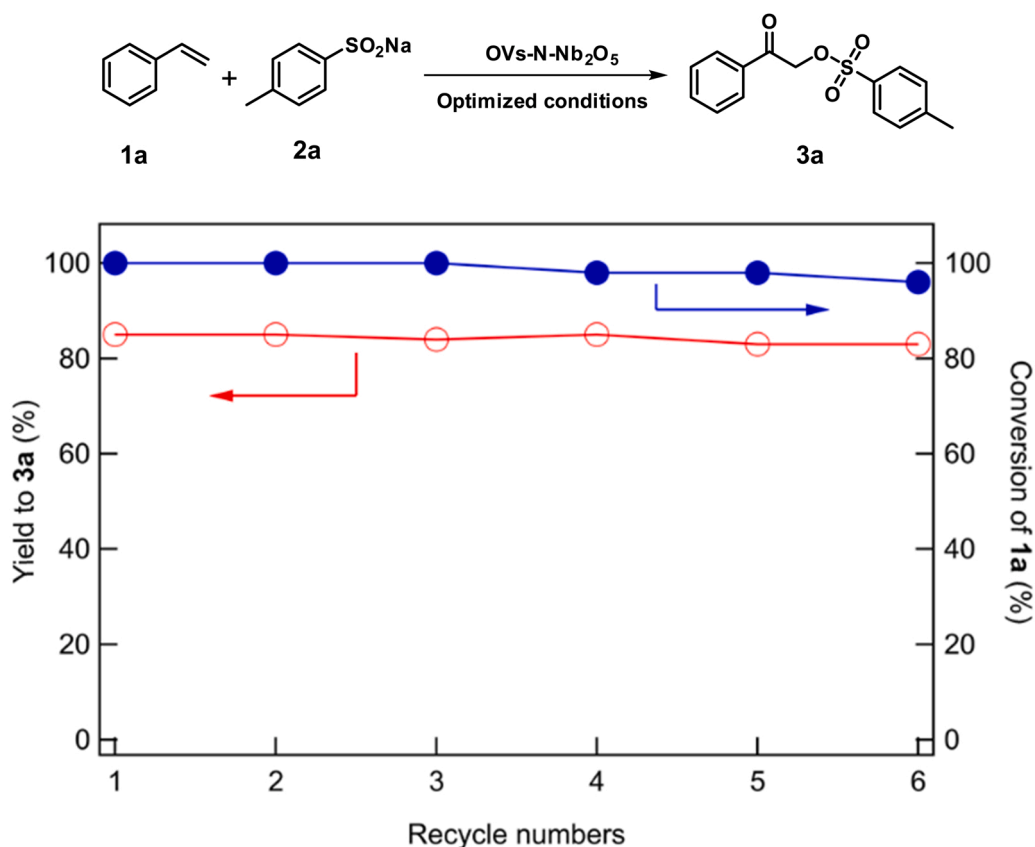


Fig. 4. Recyclability of the catalyst OV-Nb<sub>2</sub>O<sub>5</sub>.

### 3.2. Photoelectrochemical properties of OV-Nb<sub>2</sub>O<sub>5</sub>

The diffuse reflectance UV/Vis spectroscopy (DRS) (Fig. 3a) shows an absorbance edge at approximately 430 nm. Compared to the pristine Nb<sub>2</sub>O<sub>5</sub>, a notably improved light absorbance is observed, and the absorbance edge has a distinct red shift from 365 to 430 nm upon N-doping. Calculated from the Tauc plots (Fig. 3b), the corresponding band gap energy is greatly narrowed from 3.40 eV for the pristine Nb<sub>2</sub>O<sub>5</sub> to 2.90 eV for OV-Nb<sub>2</sub>O<sub>5</sub>. These observations indicate a change of energy band structure by N atoms substitution in the lattice of Nb<sub>2</sub>O<sub>5</sub>, which is beneficial for more efficient utilization of visible light, consequently leading to an improved photocatalytic activity. The steady-state photoluminescence (PL) spectroscopy (Fig. 3c) shows that the fluorescence intensity for OV-Nb<sub>2</sub>O<sub>5</sub> is markedly reduced in comparison with the pristine Nb<sub>2</sub>O<sub>5</sub>, indicating an enhanced charge extraction and greatly suppressed recombination of the photogenerated electron-hole pairs. Besides, the onset of photoluminescence wavelength has a red-shift, corroborating the narrowed bandgap. The efficient charge separation efficiency in turn increased the lifetime of the charge carriers of OV-Nb<sub>2</sub>O<sub>5</sub> (4.25 ns) compared to that of the pristine Nb<sub>2</sub>O<sub>5</sub> (3.51 ns) as confirmed by the time-resolved PL spectroscopy (Fig. 3d). As previously reported, the presence of OVs increases the ability to capture electrons, thereby prolonging the lifetime of charges and enhancing the use of electrons and holes in redox process [24]. Consistently, this result suggests the more long-lived photogenerated electrons on the surface of Nb<sub>2</sub>O<sub>5</sub> with abundant OVs could facilitate O<sub>2</sub> activation, thus enabling higher reaction efficiency. In addition, as shown in photocurrent response (Fig. 3e) and electrochemical impedance spectra (EIS) (Fig. 3f), OV-Nb<sub>2</sub>O<sub>5</sub> has a higher photocurrent density and smaller charge transfer resistance than the pristine Nb<sub>2</sub>O<sub>5</sub>, further proving a better separation and migration ability of photogenerated charges.

### 3.3. Photocatalytic alkene difunctionalization to $\alpha$ -sulfonyloxy ketones

The catalyst OV-Nb<sub>2</sub>O<sub>5</sub> was employed as the photocatalyst for visible-light-induced difunctionalization of alkenes with molecular oxygen as the sole oxidant at ambient conditions. For optimization of the reaction conditions, we first examined the model reaction of styrene (1a) with sodium *p*-toluenesulfonate in benzotrifluoride (BTF) in the presence of OV-Nb<sub>2</sub>O<sub>5</sub> (20 mg) under visible light irradiation (blue LEDs, 450 nm) (Table 1). After 12 h, 57% of 1a was converted, affording a mixture of  $\alpha$ -tosyloxy ketone (3a) and 2-(*p*-toluenesulfonyl)acetophenone (4a) with 3a as the major product (entry 1). Other solvents screening, including CH<sub>3</sub>CN, MeOH, DMF, 1,4-dioxane, or a mixture with water, shows that BTF was the best one (entries 2–7). Notably, the nature of solvent has a pronounced influence on the reaction activity and particularly selectivity. An important selectivity switch between 3a and 4a was observed and highly depended on protic or aprotic solvent employed for the reaction. The reason behind will be discussed later. A complete conversion of 1a with 87% selectivity to 3a was achieved when prolonging the irradiation time to 24 h under otherwise identical conditions (entry 8). Control experiments indicate that the catalyst, visible light, and oxygen are all indispensable for the reaction (entries 9–11). In sharp contrast, the pristine Nb<sub>2</sub>O<sub>5</sub> gave low reactivity (45% conversion) with relatively lower selectivity to 3a under equal conditions (entry 12), indicating that an improved photoelectrochemical property and abundant OVs caused by N-doping is significantly favorable for an enhancement in photoactivity and selectivity. Remarkably, a 5 mmol scale reaction was also feasible with a longer reaction time (60 h) under the optimized conditions (entry 13), highlighting the practicability.

After identifying the optimized reaction conditions, we proceeded to explore the generality of this alkene difunctionalization reaction (Table 2). First, various styrenes with an electronically diverse set of



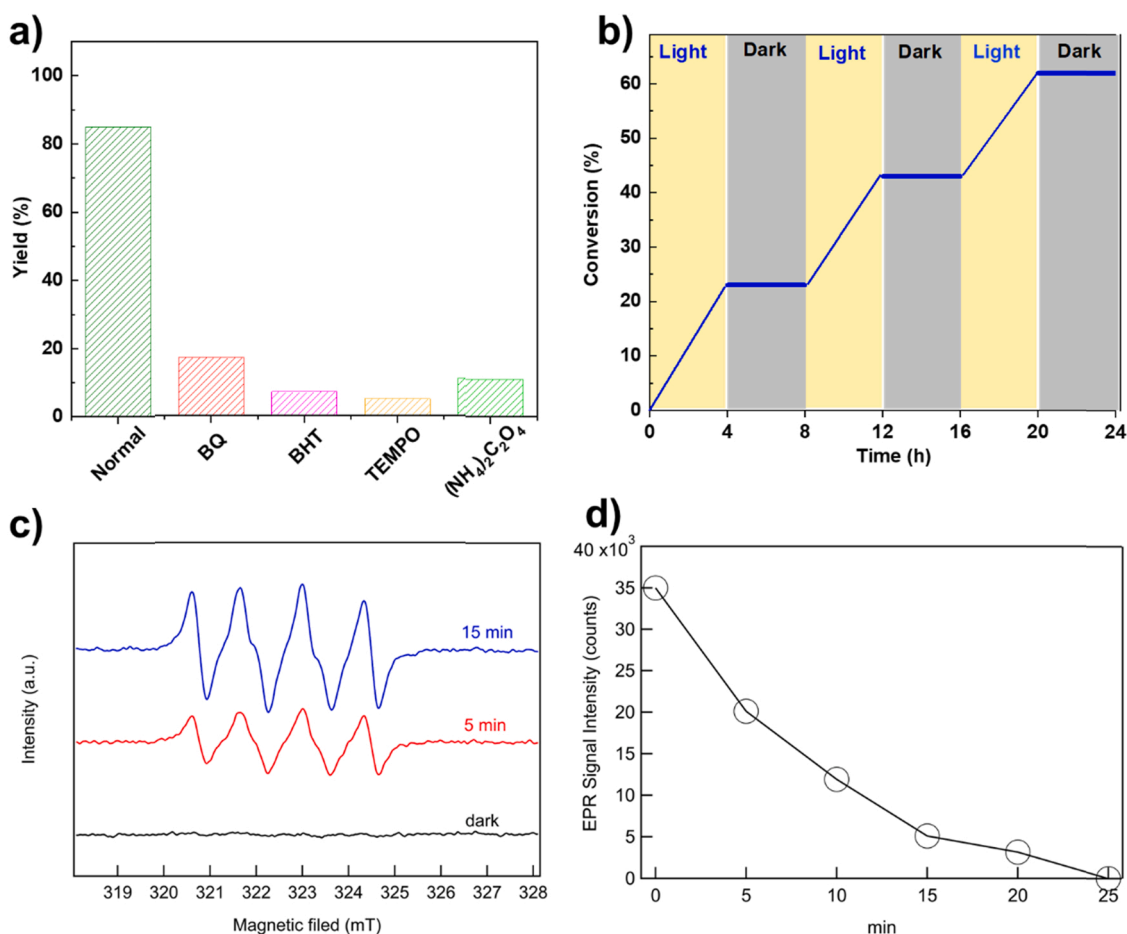


**Fig. 5.** (a) Variation in catalytic activity for the benchmark reaction with different scavengers; (b) Light switch on-off experiment for the synthesis of  $\alpha$ -sulfonyloxy ketones; (c) EPR spectra for verifying  $O_2^{\bullet-}$  as ROS, (d) the retention-time of  $O_2^{\bullet-}$  on surface of OV<sub>s</sub>-N-Nb<sub>2</sub>O<sub>5</sub>.

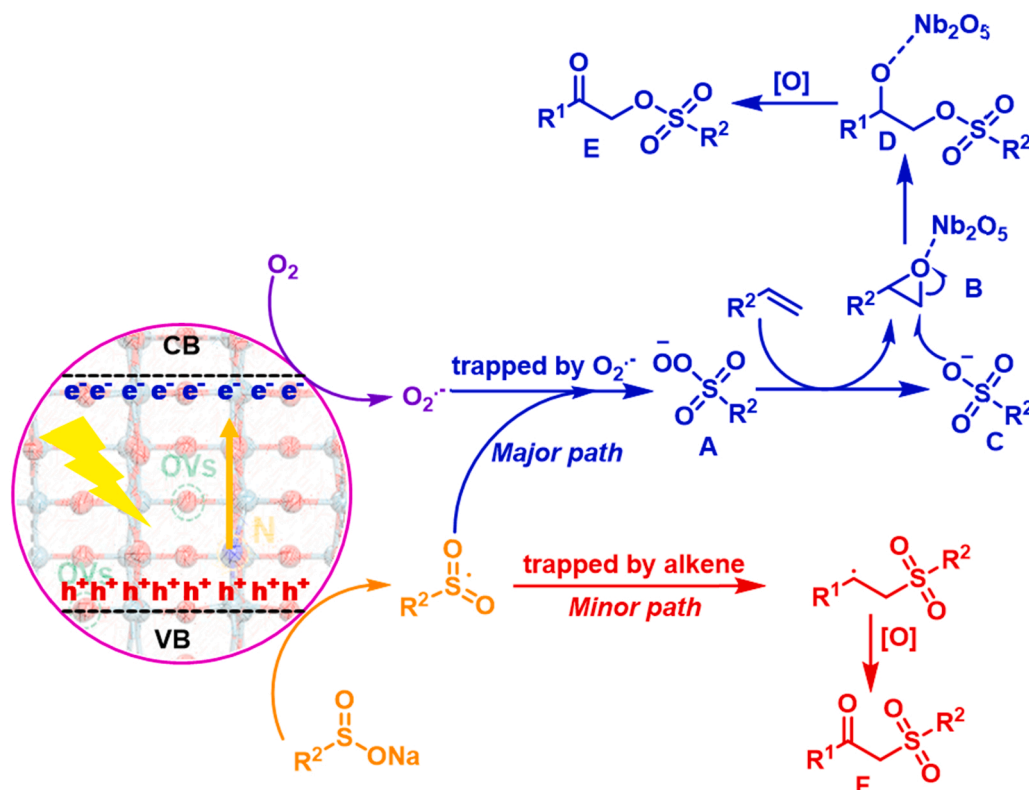
substituents, including methoxy (**1b**, **1c**), borneoxy (**1d**), cyano (**1e**), trifluoromethyl (**1f**), nitro (**1g**), and ester (**1h**) could efficiently proceed the difunctionalization with sodium *p*-toluenesulfonate to afford their corresponding  $\alpha$ -tosyloxy ketones in moderate to high yields. Styrenes bearing electron-deficient substituents generally gave a relatively lower reaction efficiency compared with the ones substituted by electron-rich groups. Second, this protocol is applicable to the hetero-aromatic alkenes, including 2-vinylfuran (**1i**), 2-vinylthiophene (**1j**), *N*-tosyl-2-vinylpyrrole (**1k**). They could be converted into their respective  $\alpha$ -tosyloxy ketones in 62–70% yields, respectively. Third, more challenging unactivated aliphatic alkenes, e.g., 4-phenyl-1-butene (**1l**), vinylcyclohexane (**1m**), and even 1,2-disubstituted cyclohexene (**1n**), worked well to afford their corresponding  $\alpha$ -tosyloxy ketones albeit with relatively lower yields. Fourth,  $\alpha$ - or  $\beta$ -site substituted internal alkenes are compatible with this protocol too, and *trans*-stilbene (**1p**), indene (**1q**),  $\beta$ -methyl styrene (**1r**), and  $\alpha$ -methyl styrene (**1s**) were effectively difunctionalized into their respective  $\alpha$ -tosyloxy ketones in high yields. Note that, in the case of  $\alpha$ -methyl styrene (**1s**), the product 2-hydroxy-2-phenylpropyl 4-methylbenzenesulfonate (**3s**) was formed. However,  $\beta$ -dimethyl substituted styrene, that is, 2-methyl-1-phenylpropene (**1o**) did not work to deliver the desired product. In this case, benzyl aldehyde was produced as the only product due to the steric hindrance. Lastly, apart from sodium *p*-toluenesulfonate, sodium benzenesulfonate could react with styrenes substituted by halogen (**1u–1x**), ethyl (**1y**), and methyl (**1z** and **1aa**) in varying position of phenyl ring, affording their corresponding  $\alpha$ -sulfonyloxy ketones in high yields. Moreover, halogen-substituted benzenesulfonate (**2c–2e**) or methylsulfonate (**2f**) could serve as radical precursors for efficient alkene difunctionalization,

highlighting the broad scope of this protocol.

The stability and reusability of the photocatalyst is of great importance for practical application. As shown in Fig. 4, the OV<sub>s</sub>-N-Nb<sub>2</sub>O<sub>5</sub> exhibited high stability and could be easily reused at least six times with negligible loss in activity, demonstrating the outstanding stability during photocatalysis. Characterizations including XRD, XPS, HR-TEM, DRS, and PL (Fig. S3–S5) for the used OV<sub>s</sub>-N-Nb<sub>2</sub>O<sub>5</sub> after 6 times recycles show no distinct changes in structure, morphology and photoelectrochemical properties as well, further verifying the excellent stability.

### 3.4. Mechanistic study

To get a better understanding of the mechanism of this reaction, a variety of control experiments were conducted. First, the benchmark reaction in the presence of specific radical scavengers under the optimized conditions was performed (Fig. 5a). The addition of *p*-benzoquinone (*p*-BQ) as a scavenger for superoxide anion radical ( $O_2^{\bullet-}$ ) results in a significant decrease in yield of **3a**, indicating the key role of the photogenerated  $O_2^{\bullet-}$  as reactive oxygen species (ROS) in the reaction. The reaction in the presence of 2,2,6,6-tetramethyl-1-piperidinyloxy (TEMPO), or 2,6-di-*tert*-butyl-4-methylphenol (BHT), as a scavenger to any involved radicals including carbon-centered radicals, nearly shut down with leaving only unreacted starting materials, strongly suggesting a radical-mediated nature. Furthermore, a considerable suppression in reactivity was observed when the reaction was conducted upon adding ammonium oxalate ((NH<sub>4</sub>)<sub>2</sub>C<sub>2</sub>O<sub>4</sub>) as scavenger photogenerated holes ( $h^+$ ). In addition, the light switch on-off experiment reveals an



Scheme 3. Proposed mechanism.

indispensable of constant light irradiation for the reaction (Fig. 5b), ruling out a radical chain process. All results make us to conclude that  $\text{O}_2^{\bullet-}$ ,  $\text{h}^+$ ,  $\text{e}^-$  and carbon-centered radicals are primarily responsible for the photocatalytic alkene difunctionalization.

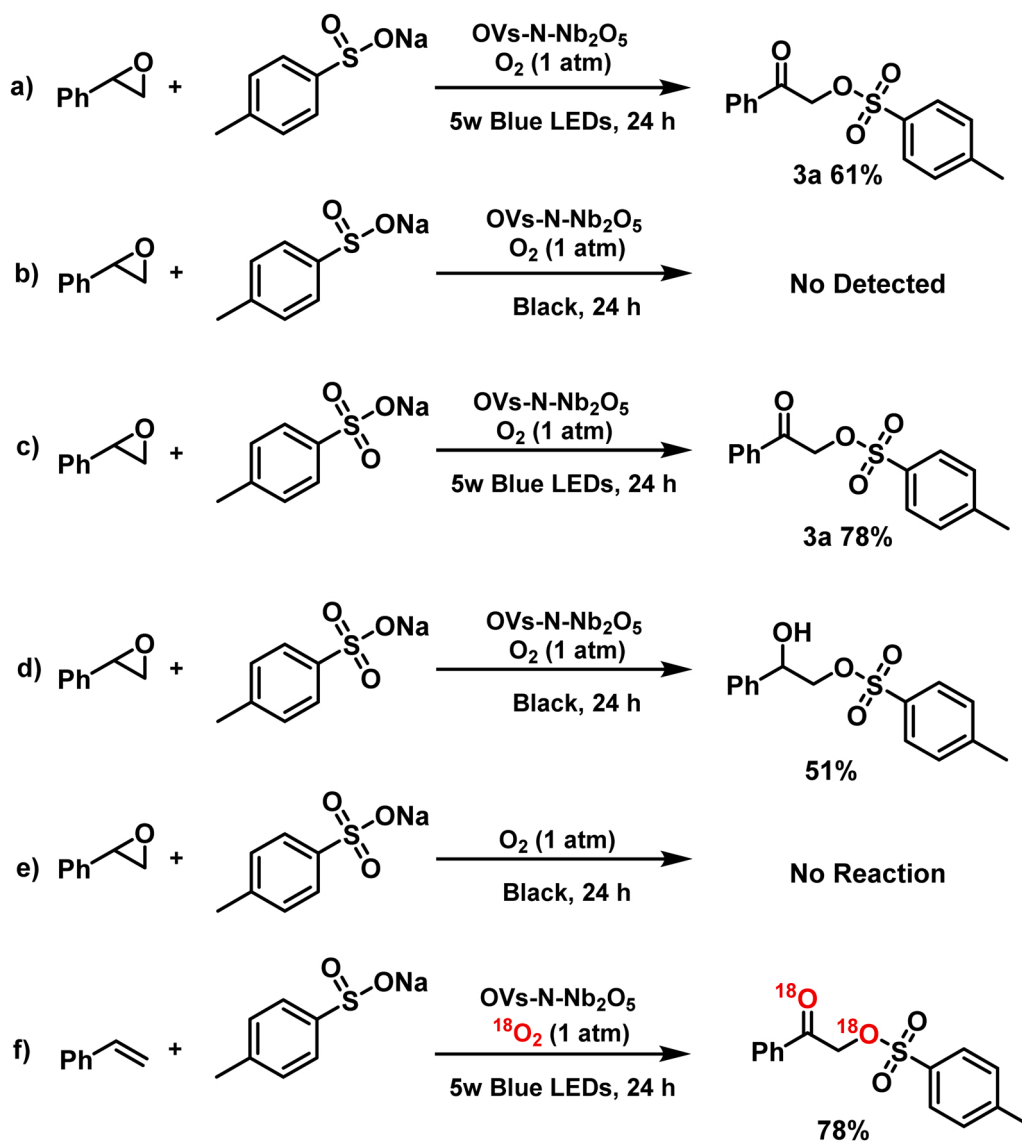
We further verify the  $\text{O}_2^{\bullet-}$  as ROS in the present reaction system by in-situ EPR experiment. As shown in Fig. 5c, a quartet peaks signal was distinctly observed in the presence of OV-Nb<sub>2</sub>O<sub>5</sub> using 5,5-dimethyl-1-pyrroline N-oxide (DMPO) as the trapping agent, which is attributable to the DMPO- $\text{O}_2^{\bullet-}$  signal [25]. No signal from DMPO- $\text{OH}$  was detected. The signal intensity gradually increased upon prolonging irradiation time. After the light was turned off, the DMPO- $\text{O}_2^{\bullet-}$  signal didn't decrease immediately and could retain for a while on the surface of OV-Nb<sub>2</sub>O<sub>5</sub> (Fig. 5d and Fig. S7). Such observations not only confirm the formation of long-lived  $\text{O}_2^{\bullet-}$  as the ROS, in agreement with the radical scavenger observation, but also indicate that the  $\text{O}_2^{\bullet-}$  could be smoothly generated and accumulated on the surface of OV-Nb<sub>2</sub>O<sub>5</sub>. Previous studies have well documented that the OV on the surface of metal oxides as active sites could facilitate  $\text{O}_2$  adsorption and activation to selectively generate long-lived  $\text{O}_2^{\bullet-}$ , which subsequently react with substrate molecules or reaction intermediates adsorbed on their surface [26]. Our findings also indicate that the OV greatly affect the concentration and life-time of the generated  $\text{O}_2^{\bullet-}$  on Nb<sub>2</sub>O<sub>5</sub>, thereby correlating the reaction activity and selectivity.

Given the unprecedented reaction selectivity to  $\alpha$ -sulfonyloxy ketones in the present study, we tentatively propose a plausible reaction pathway. As shown in Scheme 3, sodium *p*-toluenesulfinate was initially transferred into sulfonyl radical under light irradiation via single-electron transfer (SET), which was trapped by long-lived  $\text{O}_2^{\bullet-}$  accumulating on the surface to generate *p*-toluenesulfonyl peroxide acid anion (A). Next, the alkene was oxidized into epoxide intermediate (B) by A due to its strong epoxidation ability, synchronously delivering *p*-toluenesulfonyl acid anion (C) as previously reported [27,28]. Subsequently, the ring-opening of B took place in the presence of Lewis acid sites on the surface along with simultaneous attack by the generated C to

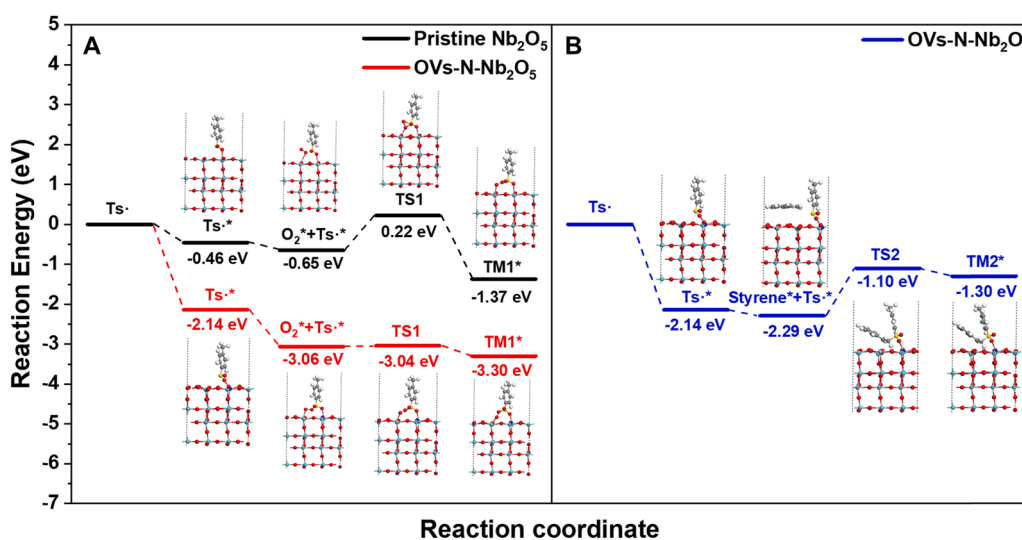
yield 2-phenylethyl benzenesulfonate anion (D) in a synergy and cascade manner. Finally, D was further oxidized toward the targeted product  $\alpha$ -sulfonyloxy ketone (E). In addition, the observation of  $\beta$ -ketone sulfone (F) as the side product, albeit with low selectivity, indicates a direct addition of sulfonyl radical to alkene is also involved.

Such proposed reaction pathways could reasonably interpret the pronounced influence of solvent on reaction activity and selectivity as observed in the condition optimization (Table 1). Since the long-lived  $\text{O}_2^{\bullet-}$  on the surface of Nb<sub>2</sub>O<sub>5</sub> has been verified to be the ROS for the reaction, its concentration and life-time in the reaction medium is paramount and has a decisive effect on driving subsequent reaction rate and reaction pathway as well, thereby determining reaction activity and product selectivity. It is reported that benzotrifluoride (BTF) has superior  $\text{O}_2$  solubility and is inert to  $\text{O}_2^{\bullet-}$  [27], which means a higher probability to generate more sulfonyl peroxide anion radical (A) via trapping of sulfonyl radical in the reaction. As a result, the reaction performed in BTF gives higher reaction efficiency and prefers to undergo the major pathway to produce 3a as the product. On the contrary, in protic solvents, e.g., MeOH, or other mixture with H<sub>2</sub>O, the generated  $\text{O}_2^{\bullet-}$  is prone to be quenched rather than being trapped by sulfonyl radical, thus driving the reaction to proceed the direct addition of sulfonyl radical to alkene and consequently resulting in excellent selectivity to 4a.

To further validate the proposed mechanism, the benchmark reaction under the optimized conditions was monitored as a function of reaction time (Fig. S8). The formation of styrene epoxide was observed at the early stage of the reaction albeit with small amount, confirming that the reaction proceeds via the formation of epoxide as the key intermediate. Subsequently, a set of control reactions were carried out using styrene epoxide as starting material (Scheme 4). Using styrene epoxide instead of styrene led to 3a in 61% yield under the optimized conditions (Scheme 4a), while 3a was not detected without light irradiation (Scheme 4b). In parallel, the reaction of styrene epoxide with sodium *p*-toluenesulfonate instead of sodium *p*-toluenesulfinate gave 3a



Scheme 4. Control experiments.

Fig. 6. Calculated free energy diagrams and adsorption configuration: (A) comparison of the pristine Nb<sub>2</sub>O<sub>5</sub> and OV-N-Nb<sub>2</sub>O<sub>5</sub> for major path; (B) OV-N-Nb<sub>2</sub>O<sub>5</sub> for minor path.

in 78% under the optimized conditions (Scheme 4c), whereas only 2-hydroxy-2-phenylethyl benzenesulfonate in 51% yield was produced without light irradiation (Scheme 4d). Furthermore, no reaction took place at all when the reaction of styrene epoxide with sodium *p*-toluenesulfonate was conducted in the absence of either light or photocatalyst (Scheme 4e). These observations further demonstrate the critical role of light and Lewis acid sites for ring-opening and subsequent oxidation to produce the targeted product  $\alpha$ -sulfonyloxy ketone. The presence of a relatively stronger Lewis acid sites on the OV<sub>s</sub>-N-Nb<sub>2</sub>O<sub>5</sub> was confirmed by pyridine adsorption FT-IR (Fig. S6). In addition, <sup>18</sup>O<sub>2</sub> labeling experiment clearly clarify that the two incorporated O atoms in  $\alpha$ -sulfonyloxy ketone originate from molecular O<sub>2</sub> (Scheme 4f and Fig. S9).

Finally, we performed density function theory (DFT) calculations to theoretically understand this unprecedented reaction pathway. Two models of Nb<sub>2</sub>O<sub>5</sub> and Nb<sub>2</sub>O<sub>5</sub> with OV<sub>s</sub> (OV<sub>s</sub>-N-Nb<sub>2</sub>O<sub>5</sub>) were constructed for comparison (Fig. S10). Theoretical calculation results reveal that OV<sub>s</sub>-N-Nb<sub>2</sub>O<sub>5</sub> has a much stronger adsorption energy for molecular O<sub>2</sub> and in-situ generated *p*-toluenesulfonyl radical than that of Nb<sub>2</sub>O<sub>5</sub>, respectively (Fig. S11). This indicates that the presence of surface OV<sub>s</sub> indeed facilitates adsorption of O<sub>2</sub> and substrate molecule, which is in consistent with the previous results [29]. The subsequent formation of *p*-toluenesulfonyl peroxide anion radical via trapping *p*-toluenesulfonyl radical by long-lived O<sub>2</sub><sup>•−</sup> accumulating on the surface of OV<sub>s</sub>-N-Nb<sub>2</sub>O<sub>5</sub> via transition state TS1 is more thermodynamically favorable and required a greatly lower activation free energy compared with that occurs on the surface of Nb<sub>2</sub>O<sub>5</sub> (0.02 vs 0.87 eV) (Fig. 6A, major path). This result, combined with a better separation and migration ability of photogenerated charges as confirmed by DRS, PL, TRPL, and EIS, answers why OV<sub>s</sub>-N-Nb<sub>2</sub>O<sub>5</sub> demonstrates a considerably higher photoactivity than Nb<sub>2</sub>O<sub>5</sub> (Table 1, entries 8 and 12). The pathway of direct addition of sulfonyl radical to alkene to form carbon centered radical (TM2\*) is also calculated. This step could take place via transition state TS2 but requires a higher activation free energy (ca. 1.19 eV) (Fig. 6B, minor path). Comparatively, the trapping of sulfonyl radical by O<sub>2</sub><sup>•−</sup> with lower activation free energy is more favorable. Such observation accounts for the excellent selectivity to  $\alpha$ -sulfonyloxy ketone.

## 4. Conclusions

In conclusion, we reported a bifunctional heterogeneous Lewis acidic Nb<sub>2</sub>O<sub>5</sub> semiconductor with abundant oxygen vacancies, serving as visible light responsible and Lewis acid catalyst, for oxidative alkene difunctionalization to access  $\alpha$ -sulfonyloxy ketones under ambient conditions in a synergistic and cascade manner. A broad range of readily available alkenes could be efficiently converted into their corresponding  $\alpha$ -sulfonyloxy ketones in high yields with good tolerance of diverse functional groups. The catalyst is highly stable and can be reused for at least 6 successive reactions with maintaining activity and selectivity. This study provides an unprecedented yet efficient method for the sustainable synthesis of  $\alpha$ -sulfonyloxy ketones via alkene difunctionalization, and also opens up an avenue to design bifunctional semiconductor materials as photocatalysts for advanced organic transformations.

## CRediT authorship contribution statement

**Tao Song:** Conceptualization, Investigation, Data curation, Formal analysis. **Chun Wang:** Methodology, Software, Resources. **Yinpan Zhang:** Formal analysis. **Xiaolin Shi:** Investigation. **Yafei Li:** Supervision. **Yong Yang:** Supervision, Funding acquisition, Writing – original draft, Writing – review & editing.

## Declaration of Competing Interest

The authors declare that they have no known competing financial interests or personal relationships that could have appeared to influence the work reported in this paper.

## Acknowledgements

We gratefully acknowledge the financial support of the National Natural Science Foundation of China (No. 22078350, 22002178), the Natural Science Foundation of Shandong Province (ZR2020KB016), and the Dalian National Laboratory for Clean Energy (DNL) Cooperation Fund, CAS (Grant No. DNL201904). Y.Y. also thanks the Royal Society (UK) for a Newton Advanced Fellowship (NAF\R2\180695).

## Appendix A. Supporting information

Supplementary data associated with this article can be found in the online version at doi:10.1016/j.apcatb.2021.120964.

## References

- (a) (For selected reviews see:) T.P. Yoon, M.A. Du Ischay, Visible light photocatalysis as a greener approach to photochemical synthesis, *Nat. Chem.* 2 (2010) 527–532;  
(b) J.-R. Chen, X.-Q. Hu, L.-Q. Lu, W.-J. Xiao, Exploration of visible-light photocatalysis in heterocycle synthesis and functionalization: reaction design and beyond, *Acc. Chem. Res.* 49 (2016) 1911–1923;  
(c) P.S. Ravelli, M. Fagnoni, Carbon-carbon bond forming reactions via photogenerated intermediates, *Chem. Rev.* 116 (2016) 9850–9913;  
(d) J. Twilton, C. Le, P. Zhang, M.H. Shaw, R.W. Evans, D.W.C. MacMillan, The merger of transition metal and photocatalysis, *Nat. Rev.* 1 (2017) 0052;  
(e) L. Marzo, S.K. Pagire, O. Reiser, B. König, Visible-light photocatalysis: does it make a difference in organic synthesis, *Angew. Chem. Int. Ed.* 57 (2018) 10034–10072.
- (a) (For selected examples see:) D.A. Nicewicz, D.W.C. MacMillan, Merging photoredox catalysis with organocatalysis: the direct asymmetric alkylation of aldehydes, *Science* 322 (2008) 77–79;  
(b) A.G. Condie, J.C. Gonzalez-Gomez, C.R.J. Stephenson, Visible-light photoredox catalysis: Aza-Henry reactions via C-H functionalization, *J. Am. Chem. Soc.* 132 (2010) 1464–1465;  
(c) S. Lin, M.A. Ischay, C.G. Fry, T.P. Yoon, Radical cation Diels-Alder cycloadditions by visible light photocatalysis, *J. Am. Chem. Soc.* 133 (2011) 19350–19353.
- (a) (For selected examples see:) H.W. Shih, M.N. Vander Wal, R.L. Grange, D.W.C. MacMillan, Enantioselective  $\alpha$ -benzylation of aldehydes via photoredox organocatalysis, *J. Am. Chem. Soc.* 132 (2010) 13600–13603;  
(b) C. Wang, K. Harms, E. Meggers, Catalytic asymmetric C<sub>sp</sub>3-H functionalization under photoredox conditions by radical translocation and stereocontrolled alkene addition, *Angew. Chem.* 128 (2016) 13693–13696;  
(c) T. Foll, J. Rehbein, O. Reiser, Ir(ppy)<sub>3</sub>-catalyzed, visible-light-mediated reaction of  $\alpha$ -chloro cinnamates with enol acetates: an apparent halogen paradox, *Org. Lett.* 20 (2018) 5794–5798.
- (a) (For selected examples see:) M. Pirtsch, S. Paria, T. Matsuno, H. Isobe, O. Reiser, [Cu(dap)<sub>2</sub>Cl] As an efficient visible-light-driven photoredox catalyst in carbon-carbon bond-forming reactions, *Chem. Eur. J.* 18 (2012) 7336–7340;  
(b) 3950–956 T. Rawner, E. Lutscher, C.A. Kaiser, O. Reiser, The different faces of photoredox catalysts: visible-light-mediated to transfer radical addition (ATRA) reactions of perfluoroalkyl oxides with styrenes and phenylacetylenes, *ACS Catal.* 8 (2018);  
(c) A. Hossain, A. Vidyasagar, C. Eichinger, C. Lankes, J. Phan, J. Rehbein, O. Reiser, Visible-light-accelerated copper (II)-catalyzed regio- and chemoselective oxo-azidation of vinyl arenes, *Angew. Chem. Int. Ed.* 57 (2018) 8288–8292;  
(d) A. Hossain, A. Bhattacharyya, O. Reiser, Copper's rapid ascent in visible-light photoredox catalysis, *Science* 364 (2019) eaav9713.
- S. Witzel, A.S.K. Hashmi, J. Xie, Light in gold catalysis, *Chem. Rev.* 121 (2021) 8868–8925.
- (a) (For selected examples see:) S.P. Pitre, C.D. McTiernan, H. Ismaili, J. C. Scaiano, Metal-free photocatalytic radical trifluoromethylation utilizing methylene blue and visible light irradiation, *ACS Catal.* 4 (2014) 2530–2535;  
(b) H. Zhang, Z. Zhan, Y. Lin, Y. Shi, G. Li, Q. Wang, Y. Deng, L. Hai, Y. Wu, Visible light photoredox catalyzed thiophosphate synthesis using methylene blue as promoter, *Org. Chem. Front.* 5 (2018) 1416–1422;  
(c) R. Ishwarbhai Patel, A. Sharma, S. Sharma, A. Sharma, Visible light-mediated applications of methylene blue in organic synthesis, *Org. Chem. Front.* 8 (2021) 1694–1718.
- (a) (For selected examples see:) M. Neumann, S. Fldner, B. König, K. Zeitler, Metal-free, cooperative asymmetric organophotoredox catalysis with visible light, *Angew. Chem. Int. Ed.* 50 (2011) 951–954;  
(b) D.P. Hari, B. König, Synthetic applications of eosin Y in photoredox catalysis, *Chem. Commun.* 50 (2014) 6688–6699;  
(c) X. Yang, Y. Zheng, L. Zheng, L.Z. Wu, C.H. Tung, B. Chen, Highly efficient and selective photocatalytic hydrogenation of functionalized nitrobenzenes, *Green Chem.* 21 (2019) 1401–1406.
- (a) (For selected examples see:) T.-Y. Shang, L.-H. Lu, Z. Cao, Y. Liu, W.-M. He, B. Yu, Recent advances of 1,2,3,5-tetrakis(carbazol-9-yl)-4,6-dicyanobenzene (4CzIPN) in photocatalytic transformations, *Chem. Commun.* 55 (2019)



- 5408–5419;
- (b) A.H. Jatoi, G.G. Pawar, F. Robert, Y. Landais, Visible-light mediated carbamoyl radical addition to heteroarenes, *Chem. Commun.* 55 (2019) 466–469;
- (c) Q.-F. Bao, Y. Xia, M. Li, Y.-Z. Wang, Y.-M. Liang, Visible-light-mediated trifluoromethylation/benzoylation of styrenes catalyzed by 4-CzIPN, *Org. Lett.* 22 (2020) 7757–7761;
- (d) Q.-Y. Meng, N. Dben, A. Studer, Cooperative NHC and photoredox catalysis for the synthesis of  $\beta$ -trifluoromethylated alkyl aryl ketones, *Angew. Chem. Int. Ed.* 59 (2020) 19956–19960.
- [9] (a) (For selected examples see:) J.B. McManus, D.A. Nicewicz, Direct C–H cyanation of arenes via organic photoredox catalysis, *J. Am. Chem. Soc.* 139 (2017) 2880–2883;
- (b) D. Moser, Y. Duan, F. Wang, Y. Ma, M.J. O'Neill, J. Cornella, Selective functionalization of aminoheterocycles by a pyrylium salt, *Angew. Chem. Int. Ed.* 57 (2018) 11035–11039;
- (c) V.A. Pistritto, M.E. Schutzbach-Horton, D.A. Nicewicz, Nucleophilic aromatic substitution of unactivated fluoroarenes enabled by organic photoredox catalysis, *J. Am. Chem. Soc.* 142 (2020) 17187–17194.
- [10] (a) (For selected examples see:) F. Su, S.C. Mathew, G. Lipner, X. Fu, M. Antonietti, S. Blechert, X. Wang, mpg-C<sub>3</sub>N<sub>4</sub>-catalyzed selective oxidation of alcohols using O<sub>2</sub> and visible light, *J. Am. Chem. Soc.* 132 (2010) 16299–16301;
- (b) I. Ghosh, J. Khamrai, A. Savateev, N. Shlapakov, M. Antonietti, B. König, Organic semiconductor photocatalyst can bifunctionalize arenes and heteroarenes, *Science* 365 (2019) 360–366;
- (c) J.-Y. Li, Y.-H. Li, M.-Y. Qi, Q. Lin, Z.-R. Tang, Y.-J. Xu, Selective organic transformations over cadmium sulfide-based photocatalysts, *ACS Catal.* 10 (2020) 6262–6280;
- (d) K. Su, H. Liu, Z. Gao, P. Fornasiero, F. Wang, Nb<sub>2</sub>O<sub>5</sub>-based photocatalysts, *Adv. Sci.* (2021) 2003156;
- (e) L. Yang, Y. Peng, X. Luo, Y. Dan, J. Ye, Y. Zhou, Z. Zou, Beyond C<sub>3</sub>N<sub>4</sub>  $\pi$ -conjugated metal-free polymeric semiconductors for photocatalytic chemical transformations, *Chem. Soc. Rev.* 50 (2021) 2147–2172;
- (f) S. Gisbertz, B. Pieber, Heterogeneous photocatalysis in organic synthesis, *ChemPhotoChem* 4 (2020) 456–475;
- (g) X. Huang, K. Zhang, B. Peng, G. Wang, M. Muhler, F. Wang, Ceria-based materials for thermocatalytic and photocatalytic organic synthesis, *ACS Catal.* 11 (2021) 9618–9678;
- (h) K. Su, H. Liu, B. Zeng, Z. Zhang, N. Luo, Z. Huang, Z. Gao, F. Wang, Visible-light-driven selective oxidation of toluene into benzaldehyde over nitrogen-modified Nb<sub>2</sub>O<sub>5</sub> Nanomeshes, *ACS Catal.* 10 (2020) 1324–1333.
- [11] L. Xiong, J. Tang, Strategies and challenges on selectivity of photocatalytic oxidation of organic substrates, *Adv. Energy Mater.* 11 (2021) 2003216–2003235.
- [12] (a) J.S. Jang, H.G. Kim, J.S. Lee, Heterojunction semiconductors: a strategy to develop efficient photocatalytic materials for visible light water splitting, *Catal. Today* 185 (2012) 270–277;
- (b) H. Wang, L. Zhang, Z. Chen, J. Hu, S. Li, Z. Wang, J. Liu, X. Wang, Semiconductor heterojunction photocatalysts: design, construction, and photocatalytic performances, *Chem. Soc. Rev.* 43 (2014) 5234–5244;
- (c) H. Zhu, X. Gan, A. McCreary, R. Lv, Z. Lin, M. Terrones, Heteroatom doping of two-dimensional materials: from graphene to chalcogenides, *Nano Today* 30 (2020) 100829–100859.
- [13] (a) S. Liang, L. Wen, S. Lin, J. Bi, P. Feng, X. Fu, L. Wu, Monolayer, monolayer HNb<sub>3</sub>O<sub>8</sub> for selective photocatalytic oxidation of benzylic alcohols with visible light response, *Angew. Chem. Int. Ed.* 53 (2014) 2951–2955;
- (b) P. Ji, X. Feng, P. Oliveres, Z. Li, A. Murakami, C. Wang, W. Lin, Strongly Lewis acidic metal-organic frameworks for continuous flow catalysis, *J. Am. Chem. Soc.* 141 (2019) 14878–14888;
- (c) Y. Dai, H. Tuysuz, Lead-free Cs<sub>3</sub>Bi<sub>2</sub>Br<sub>9</sub> perovskite as photocatalyst for ring-opening reactions of epoxides, *ChemSusChem* 12 (2019) 1–7.
- [14] (a) R.S. Varma, K.P. Naicker, D. Kumar, Can ultrasound substitute for a phase-transfer catalyst? Triphase catalysis and sonochemical acceleration in nucleophilic substitution of alkyl halides and  $\alpha$ -tosyloxyketones: synthesis of alkyl azides and  $\alpha$ -azidoketones, *J. Mol. Catal. A* 149 (1999) 153–160;
- (b) R.S. Varma, D. Kumar, Surfactant pillared clays as phase-transfer catalysts: a facile synthesis of  $\alpha$ -azidoketones from  $\alpha$ -tosyloxyketones and sodium azide, *Catal. Lett.* 53 (1998) 225–227;
- (c) B.T. Cho, W.K. Yang, O.K. Choi, Convenient synthesis of optically active 1,2-diols monosulfonates and terminal epoxides via oxazaborolidine-catalyzed asymmetric borane reduction of  $\alpha$ -sulfonyloxy ketones, *J. Chem. Soc. Perkin Trans. 1* (2001) 1204–1211;
- (d) J. Vantikomm, S. Palle, P.S. Reddy, V. Ramanatham, V.M. Khagga, Synthesis and cytotoxicity evaluation of novel 1, 4-disubstituted 1, 2, 3-triazoles via CuI catalyzed 1, 3-dipolar cycloaddition, *Eur. J. Med. Chem.* 45 (2010) 5044–5050.
- [15] (a) K.C. Nicolaou, T. Montagnon, T. Ulven, P.S. Baran, Y.L. Zhong, F. Sarabia, Novel chemistry of  $\alpha$ -tosyloxy ketones: applications to the solution- and solid-phase synthesis of privileged heterocycle and enediyne libraries, *J. Am. Chem. Soc.* 124 (2002) 5718–5728;
- (b) M.N. Vander Wal, A.K. Dilger, D.W.C. MacMillan, Development of a generic activation mode: nucleophilic  $\alpha$ -substitution of ketones via oxy-allyl cations, *Chem. Sci.* 4 (2013) 3075–3079;
- (c) C. Liu, E. Zachary Oblak, M.N. Vander Wal, A.K. Dilger, D.K. Almstead, D.W.C. MacMillan, D.W.C. MacMillan, Oxy-allyl cation catalysis: an enantioselective electrophilic activation mode, *J. Am. Chem. Soc.* 138 (2016) 2134–2137;
- (d) M. Cordier, A. Archambeau, (3+3) Cycloaddition of oxallyl cations with nitrones: diastereoselective access to 1,2-oxazinanes, *Org. Lett.* 20 (2018) 2265–2268;
- (e) J. Li, H. Shi, S. Zhang, M. Rudolph, F. Rominger, A.S.K. Hashmi, Switchable divergent synthesis in gold-catalyzed difunctionalizations of o-alkynylbenzenesulfonamides with aryl diazonium salts, *Org. Lett.* 23 (2021) 7713–7717.
- [16] (a) G.F. Koser, A.G. Relenyi, A.N. Kalos, L. Rebrovic, R.H. Wettach, One-step  $\alpha$ -tosyloxylation of ketones with [hydroxy (tosyloxy)iodo]benzene, *J. Org. Chem.* 47 (1982) 2489–2491;
- (b) J.S. Lodaya, G.F. Koser, Direct  $\alpha$ -mesyloxylation of ketones and  $\beta$ -dicarbonyl compounds with [hydroxy(mesyloxy)iodo]benzene, *J. Org. Chem.* 53 (1988) 211–214;
- (c) Y. Zhang, H. Tan, W. Liu, Synthesis of  $\alpha$ -sulfonyloxyketones via iodobenzene diacetate (PIDA)-mediated oxysulfonyloxylation of alkynes with sulfonic acids, *RSC Adv.* 7 (2017) 54017–54021;
- (d) B. Basdevant, C.Y. Legault, Enantioselective iodine(III)-mediated synthesis of  $\alpha$ -tosyloxy ketones: breaking the selectivity barrier, *Org. Lett.* 17 (2015) 4918–4921.
- [17] Y. Zhang, H. Tan, C. Yue, W. Liu, (NH<sub>4</sub>)<sub>2</sub>S<sub>2</sub>O<sub>8</sub>-mediated direct oxysulfonyloxylation of alkynes with sulfonic acids to access  $\alpha$ -sulfonyloxyketones, *ChemistrySelect* 3 (2018) 12074–12076.
- [18] (a) Y. Li, Z. Cheng, C.H. Tung, Z. Xu, Atom transfer radical addition to alkynes and enynes: a versatile gold/photoredox approach to thio-functionalized vinylsulfones, *ACS Catal.* 8 (2018) 8237–8243;
- (b) A. Hossain, S. Engl, E. Lutsker, O. Reiser, Visible-light-mediated regioselective chlorosulfonylation of alkenes and alkynes: introducing the Cu (II) complex [Cu (dap)Cl<sub>2</sub>] to photochemical ATRA reactions, *ACS Catal.* 9 (2019) 1103–1109;
- (c) X. Zhou, Z. Peng, P.G. Wang, Q. Liu, T. Jia, Atom transfer radical addition to styrenes with thiosulfonates enabled by synergetic copper/photoredox catalysis, *Org. Lett.* 23 (2021) 1054–1059.
- [19] (a) J.-J. Wang, W. Yu, Hydrosulfonylation of unactivated alkenes by visible light photoredox catalysis, *Org. Lett.* 21 (2019) 9236–9240;
- (b) S.M. Hell, C.F. Meyer, A. Misale, J.B.I. Sap, K.E. Christensen, M.C. Willis, A. Trabanco, V. Gouverneur, Hydrosulfonylation of alkenes with sulfonyl chlorides under visible light activation, *Angew. Chem. Int. Ed.* 132 (2020) 11717–11723;
- (c) Y. Zheng, Y. You, Q. Shen, J. Zhang, L. Liu, X.-H. Duan, Visible-light-induced anti-Markovnikov hydrosulfonylation of styrene derivatives, *Org. Chem. Front.* 7 (2020) 2069–2074.
- [20] (a) N. Zhang, D. Yang, W. Wei, L. Yuan, Y. Cao, H. Wang, Metal-free iodine-mediated synthesis of vinyl sulfones at room temperature using water as solvent, *RSC Adv.* 5 (2015) 37013–37018;
- (b) B. Aegurla, R.K. Peddinti, Metal-free sulfonylation of  $\alpha,\beta$ -conjugated systems by using sulfonyl hydrazides, *Asian J. Org. Chem.* 7 (2018) 946–954.
- [21] (a) Q. Lu, J. Zhang, F. Wei, Y. Qi, H. Wang, Z. Liu, A. Lei, Aerobic oxysulfonylation of alkenes leading to secondary and tertiary  $\beta$ -hydroxysulfones, *Angew. Chem. Int. Ed.* 125 (2013) 7297–7300;
- (b) K. Choudhuri, T.K. Achar, P. Mal, Iodine-triggered aerobic oxysulfonylation of styrenes, *Adv. Synth. Catal.* 359 (2017) 3566–3576;
- (c) Y. Yuan, Y. Cao, Y. Lin, Y. Li, Z. Huang, A. Lei, Electrochemical oxidative alkoxylation of alkenes using sulfonyl hydrazides and alcohols with hydrogen evolution, *ACS Catal.* 8 (2018) 10871–10875;
- (d) J. Wen, X. Yang, Z. Sun, J. Yang, P. Han, Q. Liu, H. Dong, M. Gu, L. Huang, H. Wang, Biomimetic photocatalytic sulfonation of alkenes to access  $\beta$ -ketosulfones with single-atom iron site, *Green Chem.* 22 (2020) 230–238.
- [22] H. Huang, C. Wang, J. Huang, J. Wang, Y. Du, P. Yang, Structure inherited synthesis of N-doped highly ordered mesoporous Nb<sub>2</sub>O<sub>5</sub> as robust catalysts for improved visible light photoactivity, *Nanoscale* 6 (2014) 7274–7278.
- [23] (a) S.B.T. Tran, H. Choi, S. Oh, J.Y. Park, Defective Nb<sub>2</sub>O<sub>5</sub>-supported Pt catalysts for CO oxidation: promoting catalytic activity via oxygen vacancy engineering, *J. Catal.* 375 (2019) 124–134;
- (b) X.H. Chen, X.L. Li, L.L. Wu, H.C. Fu, J. Luo, L. Shen, Q. Zhang, J.L. Lei, H. Q. Luo, N.B. Li, Nb<sub>2</sub>O<sub>5</sub>-Ni<sub>3</sub>N heterojunction tuned by interface oxygen vacancy engineering for the enhancement of electrocatalytic hydrogen evolution activity, *J. Mater. Chem. A* 9 (2021) 11563–11572.
- [24] (a) Z. Miao, G. Wang, X. Zhang, L. Dong, Oxygen vacancies modified TiO<sub>2</sub>/Ti<sub>3</sub>C<sub>2</sub> derived from MXenes for enhanced photocatalytic degradation of organic pollutants: the crucial role of oxygen vacancy to schottky junction, *Appl. Surf. Sci.* 528 (2020) 146929–146940;
- (b) Y. Xu, H. Li, B. Sun, P. Qiao, L. Ren, G. Tian, Jiang, B.K. Pan, W. Zhou, Surface oxygen vacancy defect-promoted electron-hole separation for porous defective ZnO hexagonal plates and enhanced solar-driven photocatalytic performance, *Chem. Eng. J.* 379 (2020) 122295–122305;
- (d) Q. Wang, W. Wang, L. Zhong, D. Liu, X. Cao, F. Cui, Oxygen vacancy-rich 2D/2D BiOCl-g-C<sub>3</sub>N<sub>4</sub> ultrathin heterostructure nanosheets for enhanced visible-light-driven photocatalytic activity in environmental remediation, *Appl. Catal. B Environ.* 220 (2018) 290–302.
- [25] (a) A. Samuni, A. Samuni, H.M. Swartz, The cellular-induced decay of DMPO spin adducts of OH and O<sup>•−</sup>, *Free Radic. Biol. Med.* 6 (1989) 179–183;
- (b) A. Bosnjakovic, S. Schlick, Spin trapping by 5,5-dimethylpyrrolidine-N-oxide in Fenton media in the presence of nafion perfluorinated membranes: limitations and potential, *J. Phys. Chem. B* 110 (2006) 10720–10728.
- [26] (a) J. Yang, S. Hu, Y. Fang, S. Hoang, L. Li, W. Yang, Z. Liang, J. Wu, J. Hu, W. Xiao, C. Pan, Z. Luo, J. Ding, L. Zhang, Y. Guo, Oxygen vacancy promoted O<sub>2</sub> activation over perovskite oxide for low-temperature CO oxidation, *ACS Catal.* 9 (2019) 9751–9763;
- (b) Y. Li, W. Zhang, J. Niu, Y. Chen, Mechanism of photogenerated reactive oxygen species and correlation with the antibacterial properties of engineered metal-oxide nanoparticles, *ACS Nano* 6 (2012) 5164–5173;

- (c) Y. Huang, Y. Yu, Y. Yu, B. Zhang, Oxygen vacancy engineering in photocatalysis, *Sol. RRL* 4 (2020) 2000037–2000051.
- [27] (a) R. Kluge, M. Schulz, S. Liebsch, Diastereoselective epoxidation of olefins by organo sulfonic peracids, II, *Tetrahedron* 52 (1996) 2957–2976;  
(b) Z. Yan, F. Zeng, W. Tian, Y. Epoxidation of olefins with para-toluenesulfonyl fluoride/hydrogen peroxide/base system, *Chin. J. Org. Chem.* 29 (2009) 115–118.
- [28] (a) N. Zhang, Z. Fu, Y.J. Xu, A facile and green approach to synthesize Pt@CeO<sub>2</sub> nanocomposite with tunable core-shell and yolk-shell structure and its application as a visible light photocatalyst, *J. Mater. Chem.* 21 (2011) 8152–8159;  
(b) M. Xie, X. Dai, S. Meng, X. Fu, S. Chen, Selective oxidation of aromatic alcohols to corresponding aromatic aldehydes using In<sub>2</sub>S<sub>3</sub> microsphere catalyst under visible light irradiation, *Chem. Eng. J.* 245 (2014) 107–116;  
(c) B. Zhang, J. Li, Y. Gao, R. Chong, Z. Wang, L. Guo, X. Zhang, C. Li, To boost photocatalytic activity in selective oxidation of alcohols on ultrathin Bi<sub>2</sub>MoO<sub>6</sub> nanoplates with Pt nanoparticles as cocatalyst, *J. Catal.* 345 (2017) 96–103.
- [29] (a) H. Li, J. Shang, Z. Yang, W. Shen, Z. Ai, Z. Zhang, Oxygen vacancy associated surface fenton chemistry: surface structure dependent hydroxyl radicals generation and substrate dependent reactivity, *Environ. Sci. Technol.* 51 (2017) 5685–5694;  
(b) Y. Hinuma, T. Toyao, T. Kamachi, Z. Maeno, S. Takakusagi, S. Furukawa, I. Takigawa, K. Shimizu, Density functional theory calculations of oxygen vacancy formation and subsequent molecular adsorption on oxide surfaces, *J. Phys. Chem. C* 122 (2018) 29435–29444;  
(c) 4774–478 Y. Zheng, R. Zhang, L. Zhang, Q. Gu, Z.A. Qiao, A resol-assisted cationic coordinative co-assembly approach to mesoporous ABO<sub>3</sub> perovskite oxides with rich oxygen vacancy for enhanced hydrogenation of furfural to furfuryl alcohol, *Angew. Chem. Int. Ed.* 60 (2021).